Atmos. Meas. Tech., 18, 5607–5618, 2025
https://doi.org/10.5194/amt-18-5607-2025

Atmospheric Measurement Techniques
Open Access
EGU

EarthCARE's cloud profiling radar antenna pointing correction using surface Doppler measurements

Bernat Puigdomènech Treserras[1], **Pavlos Kollias**[1,2], **Alessandro Battaglia**[3,4], **Simone Tanelli**[5], **and Hirotaka Nakatsuka**[6]

[1]Department of Atmospheric and Oceanic Science, McGill University, Montreal, H3A 0B9, QC, Canada
[2]School of Marine and Atmospheric Sciences, Stony Brook University, Stony Brook, NY 11790, NY, USA
[3]Department of Environment, Land and Infrastructure Engineering (DIATI), Politecnico of Torino, Turin, Italy
[4]Department of Physics and Astronomy, University of Leicester, Leicester, UK
[5]Jet Propulsion Laboratory, California Institute of Technology, Pasadena, CA, USA
[6]Japan Aerospace Exploration Agency, 305-8505 2 Chome–1–1, Sengen, Tsukuba, Ibaraki, Japan

Correspondence: Bernat Puigdomènech Treserras (bernat.puigdomenech-treserras@mcgill.ca)

Received: 8 April 2025 – Discussion started: 15 April 2025
Revised: 25 June 2025 – Accepted: 26 July 2025 – Published: 21 October 2025

Abstract. The Earth Cloud Aerosol and Radiation Explorer (EarthCARE) mission, a joint effort between the European Space Agency (ESA) and the Japan Aerospace Exploration Agency (JAXA), aims to advance our understanding of aerosols, clouds, precipitation, and radiation using a comprehensive payload of active and passive sensors. A key component of the payload is the 94 GHz cloud profiling radar (CPR), which provides the first-ever Doppler velocity measurements collected from space. Accurate knowledge of the CPR antenna pointing is essential for ensuring high-quality CPR Doppler velocity measurements. This study focuses on the geolocation assessment and antenna mispointing corrections during EarthCARE's commissioning phase and beyond, using Earth's surface Doppler velocity measurements collected over the first 9 months of the mission. While the instrument footprint is proven to be properly geolocated within about 100 m, surface Doppler velocity observations reveal mispointing trends influenced by solar illumination cycles and thermoelastic distortions on the antenna. Correcting these effects significantly reduces biases, ensuring better Doppler velocity measurements, essential for understanding cloud microphysics and dynamics. The results, validated through the analysis of Doppler velocities in ice clouds, underline the critical role of pointing corrections for the success of the EarthCARE mission.

1 Introduction

The Earth Cloud Aerosol and Radiation Explorer (EarthCARE) mission (Wehr et al., 2023), a joint satellite mission by the European Space Agency (ESA) and the Japan Aerospace Exploration Agency (JAXA), was successfully launched on 28 May 2024. The mission aims to deliver groundbreaking observations of aerosols, clouds, precipitation, and radiation, advancing our understanding of their properties and intricate interactions that will help improve climate models and weather forecasting (Illingworth et al., 2015). As the most sophisticated ESA Earth Explorer mission to date, the EarthCARE satellite is equipped with two active (radar and lidar) and two passive (spectral and broadband) radiometer sensors. The onboard radar is a high-sensitivity 94 GHz cloud profiling radar (CPR) with Doppler capabilities, enabling the first-ever collection of Doppler velocity measurements from a spaceborne radar system (Kollias et al., 2014; Battaglia et al., 2020).

During the commissioning phase, which included the first 6 months following its launch, several activities were performed to finalize and ensure the proper operation of the satellite's payloads according to the mission requirements. These activities include ground segment checks for data acquisition, processing, and distribution, as well as the verification of health and functionality, in-orbit calibration, characterization, and performance verification of the instruments.

The experience gained by the successful CloudSat mission by the National Aeronautics and Space Administration (NASA), the Canadian Space Agency (CSA), and the US Air Force (USAF) (Stephens et al., 2002) and its cloud profiling radar (Tanelli et al., 2008) provided a wealth of information on how to address several aspects of the initial CPR evaluation during the commissioning phase. This includes methods to calibrate CPR science data using the ocean surface normalized radar cross section (Tanelli et al., 2008; Battaglia and Kollias, 2015a) and the CloudSat-derived climatology of ice clouds (Battaglia and Kollias, 2015b); ground clutter removal (Burns et al., 2016); and path-integrated attenuation (PIA) estimation (Haynes et al., 2009).

On the other hand, the EarthCARE CPR Doppler velocity measurements are new. The quality of these measurements is affected by three main factors (Kollias et al., 2022): intrinsic noise due to the signal decorrelation (spectral broadening) introduced by the platform motion, residual errors in correcting Doppler velocity biases introduced by non-uniform beam filling (NUBF) (Tanelli et al., 2002; Kollias et al., 2022; Sy et al., 2014), and outstanding biases and errors due to uncertainty in the CPR antenna pointing characterization (Tanelli et al., 2005; Battaglia and Kollias, 2015b). The treatment of the two first terms (spectral broadening and NUBF) in the CPR L2a data products is described in Kollias et al. (2023). Here, we focus on two critical activities related to the third term, conducted during the commissioning phase and extending a few months beyond: the geolocation and the assessment of the off-nadir antenna pointing angle along the orbital track, especially important to determine the quality of the Doppler velocity measurements.

A comparable pointing characterization has been documented in the Aeolus mission, launched in August 2018, which was the first satellite to provide global wind profiles using Doppler wind lidar (Kanitz et al., 2019; Reitebuch et al., 2020). Aeolus exhibited complex, seasonally modulated wind biases caused by thermoelastic deformations of its primary mirror. These deformations were driven by variations in Earth's infrared albedo (i.e., outgoing longwave radiation), which in turn depended on atmospheric and illumination conditions. The resulting structural changes affected the angle of incidence and divergence on the Fabry–Perot and Fizeau interferometers used to retrieve Doppler shifts from Rayleigh and Mie scattering. These effects introduced horizontal line-of-sight (HLOS) wind biases along the orbit, sometimes exceeding several meters per second (Rennie et al., 2021; Weiler et al., 2021).

In contrast, the EarthCARE CPR pointing biases discussed in this study arise from antenna mispointing primarily induced by direct solar illumination and subsequent shading of the antenna structure. While the mechanisms differ, both cases share the common influence of solar-induced distortions. Notably, Aeolus demonstrated that wind bias could be correlated with onboard temperature sensors mounted on the mirror's backside (Weiler et al., 2021), leading to a major breakthrough in bias correction strategies (Rennie et al., 2021) and highlighting the potential value of integrating temperature telemetry into satellite mispointing correction techniques.

In this study, both the geolocation and antenna pointing characterization are derived from surface measurements collected over natural targets between the months of June 2024 and June 2025, the geolocation techniques described in Puigdomènech Treserras and Kollias (2024), and the C-APC product described in Kollias et al. (2023). Although thermistors are installed on the backside of the CPR antenna and were used during pre-launch tests to model thermal deformation, the telemetry data are not publicly available and are not used in the present study. Instead, we adopt an observation-based approach that leverages the Earth's surface as a stable reference. The results presented here are further validated through a comparison of the pointing effects on the climatology of Doppler velocities in ice clouds.

2 Geolocation

The accurate determination of the precise location on Earth's surface and atmosphere corresponding to signals received by the CPR instrument is essential for their interpretation. Furthermore, because one of the strengths of the EarthCARE mission is the synergistic use of multisensor observations, the CPR measurements must be properly geolocated in order to ensure an effective integration with the signals from all other sensors. These measurements are combined in synergistic algorithms like AC-TC (Irbah et al., 2023), ACM-CAP (Mason et al., 2023), and ACM-COM (Cole et al., 2023).

Here, the geolocation assessment is performed using the techniques described in Puigdomènech Treserras and Kollias (2024), based on the positions of known natural targets, such as significant elevation gradients and coastlines over more than 140 domains of $2^\circ \times 2^\circ$ distributed around the globe. For significant elevation gradients, the assessment is performed by comparing the instrument's surface detection height to a reference digital elevation model (DEM). To do this, small displacements are systematically applied to the CPR geolocation coordinates in both along- and cross-track directions when projecting the detected surface onto the DEM. These displacements correspond to different possible geolocation offsets, as any pointing results in a lateral shift of the projected footprint on the ground. The step sizes are chosen such that the corresponding horizontal shifts match the DEM resolution (1 arcsec), ensuring optimal sampling for the analysis. The absolute geolocation is determined by the shift that maximizes the correlation between the instrument and the DEM-estimated surface height. For coastlines, the analysis leverages the fact that land and ocean surfaces exhibit distinct normalized radar cross-section signatures, resulting in sharp surface signal gradients at land–ocean transitions. These transitions, detected in the CPR surface signal, provide

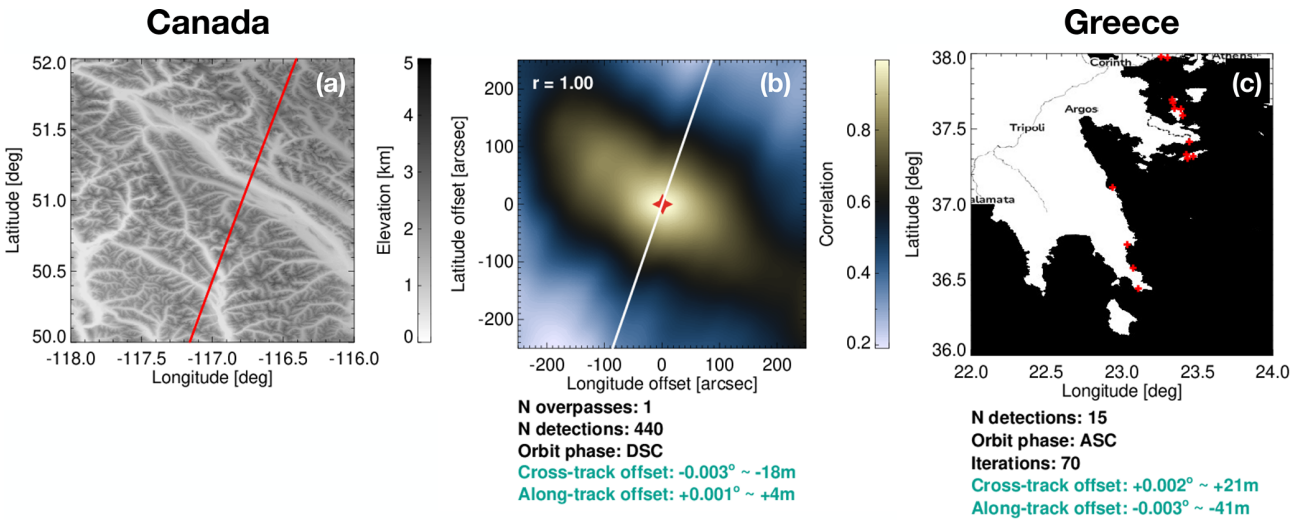

Figure 1. EarthCARE CPR geolocation assessment using significant elevation gradients and coastlines. Panels **(a)** and **(b)** illustrate an example based on significant elevation gradients in a mountainous region of British Columbia, Canada. Panel **(a)** shows the selected 2×2 domain, with the red line representing one of the EarthCARE overpasses. Panel **(b)** depicts the correlation analysis used to estimate the optimal geolocation offset for the full set of surface detections and the entire domain shown in panel **(a)**, with the white line representing the satellite path, in descending orbit, and the red filled star denoting the final estimated geolocation offset. Panel **(c)** presents the coastline-based geolocation assessment in a region near the Greek Islands. The red dots represent clear coastline detections, aggregated from multiple overpasses between August and November 2024. Unlike the elevation-gradient method, the coastline analysis is based on direct minimization of spatial distances between the detected transitions and the reference coastline map, rather than a 2D scan over a grid of possible offsets. The base map is © OpenStreetMap contributors 2015, distributed under the Open Data Commons Open Database License (ODbL) v1.0.

coastline geolocation markers. Then, through a minimization approach, the absolute geolocation is determined by minimizing the error between a collection of coastline detections and a reference map. The primary limitation of this approach is that it requires sufficient sampling of coastline crossings to ensure statistical robustness, which is why detections over several months must be aggregated.

During the commissioning phase, an extensive analysis of the data collected over the specified set of regions of interest confirmed that the CPR instrument is accurately geolocated, with overall pointing errors remaining below 100 m – 5 times better than the initially specified requirements by ESA.

Figure 1 illustrates two examples of the geolocation analysis: one over a mountainous region of British Columbia, Canada, and another over the southern coastlines of Greece. The first analysis, illustrated in Fig. 1a and b, utilizes the significant elevation gradients technique based on a single overpass, which has proven sufficient for performing the geolocation assessment. This technique benefits from the abundance of surface detections within the domain given by the along-track resolution of 500 m and the vertical sampling resolution of 100 m. In contrast, the coastline geolocation assessment, illustrated in Fig. 1c, is derived from a collection of detections spanning 4 months of data used in the analysis, i.e., August to November 2024. This approach is necessary because the coastline technique typically identifies only one or a few crossings within the domain, which is not enough to assess the instruments' geolocation. Although the effect of aggregating data over several months could, in principle, smooth out geolocation variations, the technique is based on the assumption that such variations are sufficiently small, and the resulting estimates are expected to remain stable over timescales of a few months.

Overall statistics of the geolocation assessment are presented in Fig. 2, which shows that the average along- and cross-track mispointing angles are 0.002 and 0.008° for ascending orbits and −0.014 and −0.007° for descending orbits, respectively. At a satellite altitude of 395 km, a mispointing error of 0.01° corresponds to a geolocation error of approximately 69 m. Although the geolocation techniques have inherent accuracy limits, as described in Puigdomènech Treserras and Kollias (2024), the results show the presence of along- and cross-track biases that are well within the pointing requirements.

3 Surface Doppler velocity

Although the CPR instrument footprint is geolocated within the specified requirements ($\sim 1/10$ of its footprint), this requirement is not sufficient to ensure that no Doppler velocity biases are introduced due to antenna mispointing. At the velocity of the satellite, about $7.6\,\mathrm{km\,s^{-1}}$, a minimal mispointing error of 0.01° in the along-track direction translates into a Doppler velocity bias of about $1.33\,\mathrm{m\,s^{-1}}$. Therefore,

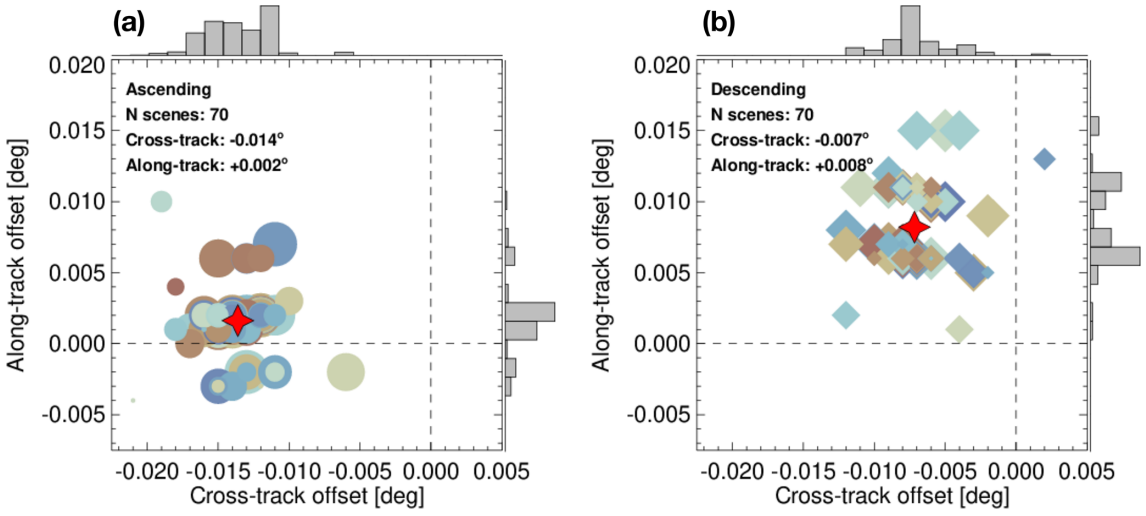

Figure 2. Combined global geolocation statistics of the EarthCARE CPR for data collected from August to November 2024: **(a)** ascending and **(b)** descending parts of the orbit. Each symbol represents an individual domain where the geolocation is assessed, with the symbol size being indicative of the number of overpasses. Distinctive colors identify different domains, while filled stars denote the averages. The dashed lines denote the perfect geolocation point (0°).

meeting the geolocation requirements is not satisfactory for achieving good Doppler measurements. Thus, a more detailed assessment is required to identify and possibly correct any possible Doppler velocity bias due to along-track antenna mispointing. To evaluate this further, the Doppler velocity measurements are analyzed to verify if there is any residual mispointing contaminating the data.

Fortunately, the Earth's surface, which typically represents a disturbance for the atmospheric signal, can be used as a Doppler signal reference target. For a Doppler radar pointing near nadir, when a beam-limited approximation is valid, assuming that the antenna footprint is several hundreds of meters wide, it can be assumed that the average vertical velocity of the surface (be it ocean, vegetated land, or something else) is generally 0 on average. Therefore, any departure from the expected $0\,\mathrm{m\,s^{-1}}$ velocity, after correcting any potential NUBF effects, indicates a potential antenna mispointing (Testud et al., 1995; Kobayashi and Kumagai, 2003; Tanelli et al. 2005; Battaglia and Kollias, 2015a; Scarsi et al., 2024).

The analysis of surface Doppler velocities is performed globally, without separating land and ocean scenes, on individual orbits to ensure both temporal and spatial consistency in the data. For each orbit, surface measurements are examined within 250 km along-track running windows, calculating the averages and standard deviations for each window. To provide a robust summary of the data, the median of these statistics is computed for each position globally, gridded at a resolution of $1^\circ \times 1^\circ$ latitude and longitude.

This method is chosen for several reasons. First, using individual segments allows for a clear separation of measurements in time and space, reducing potential biases from overlapping data. After examining the data at different window lengths, the 250 km window (i.e., about 32 s of integration time) is chosen as an optimal balance: it is long enough to smooth out small-scale variability, such as noise, while still preserving meaningful large-scale trends in the Doppler measurements. Finally, employing the median of the averages and standard deviations effectively minimizes the impact of outliers, providing a reliable representation of the overall Doppler velocity average and variability while maintaining robustness to noise and anomalies.

The spatial average and variability of the surface Doppler velocity (i.e., the Doppler velocity corresponding to the surface range) for the period from August to November 2024 is shown in Fig. 3a and b. The surface range is identified in the CPR L1b surface detection algorithm, which applies a parabolic fitting of the reflectivity profile near the surface. Here, the surface Doppler velocity corresponds to the Doppler velocity at the integer range bin reported by this detection. The corresponding sea ice coverage and snow-covered land areas derived from the ECMWF model are shown in Fig. 3c. Variance in the measured surface Doppler velocity arises not only from the surface type but also from spectral broadening, which results from the convolution of the CPR antenna pattern with the velocity gradients within the radar footprint due to the satellite's rapid motion (Sy and Tanelli, 2022). Additionally, the CPR pulse-repetition frequency (PRF) configuration, shown in Fig. 3d, determines the number of pulses transmitted per second by the CPR and thus the number of samples used to estimate the surface Doppler velocity, affecting its uncertainty. The higher the PRF value, the lower the Doppler velocity uncertainty (Kollias et al., 2014). The depth of the atmospheric layer we

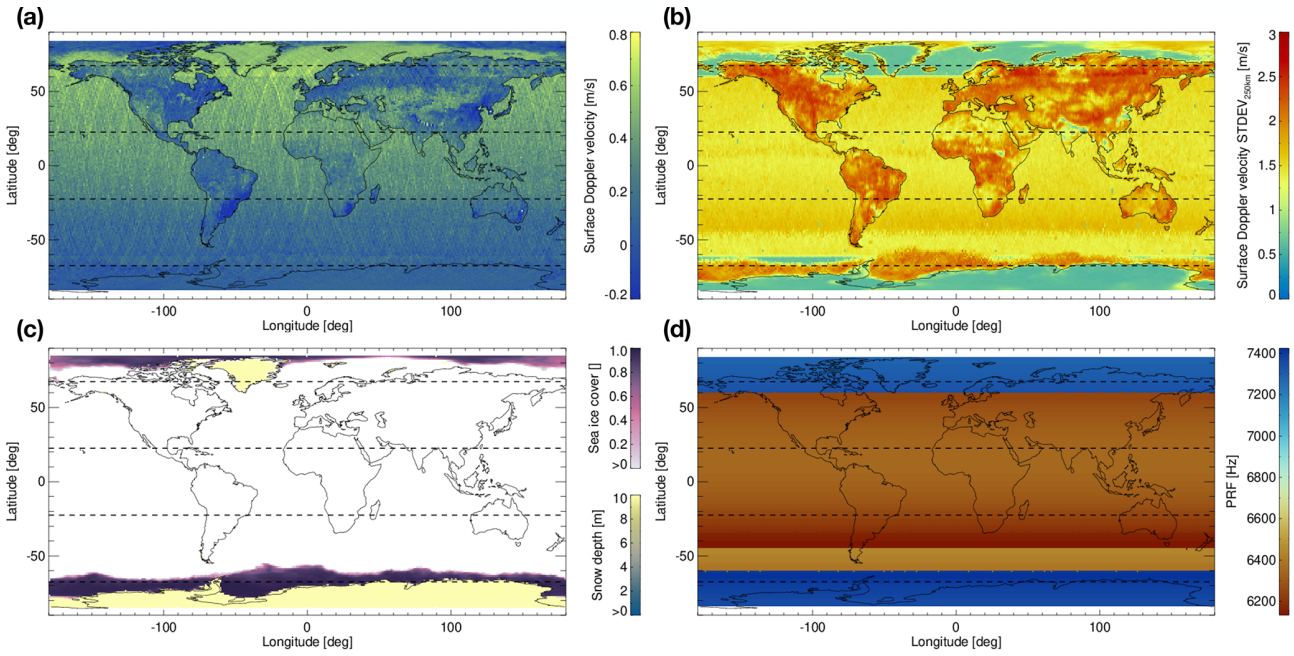

Figure 3. Panels **(a)** and **(b)** depict the global surface Doppler velocity tendency and variability, represented by the median of the mean and standard deviation values, both calculated from orbit-to-orbit measurements within a 250 km along-track window collected from August to November 2024. Panel **(c)** depicts the ECMWF average model sea ice cover and snow depth for the same period, and panel **(d)** shows the default variable EarthCARE CPR pulse-repetition frequency (PRF) configuration, which changes as a function of the latitude. The horizontal dashed lines are plotted to indicate the boundaries of the orbit's segments, defined by frame IDs: (A) +22.5 to −22.5° ascending, (B) +22.5 to +67.5° ascending, (C) +67.5° ascending to +67.5° descending, (D) +67.5 to +22.5° descending, (E) +22.5 to −22.5° descending, (F) −22.5 to −67.5° descending, (G) −67.5° descending to −67.5° ascending, and (H) −67.5° to −22.5° ascending.

want to sample (troposphere) is the only practical limiting factor. As a result, the PRF progressively increases at higher latitudes as the depth of the troposphere decreases.

While the results highlighted in Fig. 3 do not differentiate between ascending and descending orbits, Fig. 3a already reveals a noticeable bias in surface Doppler measurements as a function of latitude, suggesting potential mispointing, especially in the Northern Hemisphere (brighter colors). In contrast, land surfaces exhibit considerable spatial variability and regional biases that deviate from the oceanic trend. These biases are not uniformly correlated with orography but are also linked to the heterogenic characteristics of the surface. At least two primary factors could contribute to this mispointing: errors in the satellite's attitude systems and thermoelastic distortions. Figure 3b depicts the surface Doppler variability, Fig. 3c depicts the ECMWF average model sea ice cover and snow depth, and Fig. 3d shows the default EarthCARE CPR PRF configuration.

One of the most notable characteristics of the surface Doppler measurements is their variability, which is dependent on the orography, surface type, and CPR PRF settings. The lowest Earth's surface Doppler velocity variability is observed over ocean and snow-covered land (e.g., Antarctica and Greenland). Flat surfaces and uniform surfaces are expected to introduce no vertical motion at nadir, whereas heterogenic and rough topography can generate heterogenous backscattering and significant terrain-induced Doppler effects due to slopes and variations in reflectivity causing NUBF effects (Manconi et al., 2025). Consequently, land regions tend to exhibit noisier measurements, with exceptions such as the deserts of Western Australia, the Sahara, and Namibia, which have relatively uniform surfaces. Sea ice, on the other hand, appears to considerably increase the measurement variability. Additionally, the high PRF settings, configured to find balance between the unambiguous range and the tropopause height (a proxy for maximum cloud top height) at different latitudes, significantly reduce the measurement variability at high latitudes (e.g., near the North Pole and Antarctica), where the PRF is at its highest, further highlighting the influence of the instrument configuration on data quality.

4 Antenna pointing correction

The clear-sky Doppler velocity measurements over the ocean (free of ice) and snow-covered land (Antarctica and Greenland) collected for all orbits from June 2024 to June 2025 are used to document the biases observed in the global climatological analysis, and in order to identify any potential antenna mispointing, other land regions are excluded from the

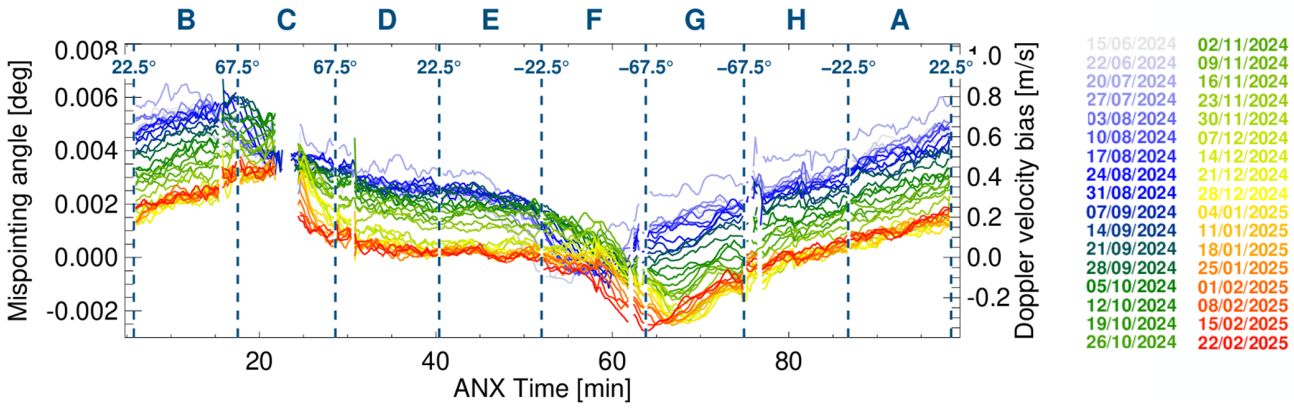

Figure 4. Weekly averaged EarthCARE CPR antenna mispointing angle as a function of the ANX time (time since ascending node crossing) derived from clear-sky surface Doppler velocity measurements collected over the sea surface (free of ice) and snow-covered land from June 2024 to June 2025. The letters on top correspond to the frame IDs, which denote the different segments of the orbit, each spanning a specific latitude and time range marked by the dashed vertical lines, with the corresponding latitude values displayed above them.

analysis because the high variability of their surface Doppler measurements compromises the precision required for mispointing detection and the integrity of the global assessment. The surface Doppler velocity measurements are corrected for NUBF effects, averaged using a 250 km running window and converted to antenna mispointing angles considering the satellite velocity. Figure 4 illustrates the resulting weekly averaged mispointing angles as a function of the ANX time (time since ascending node crossing).

The analysis presented in Fig. 4 demonstrates a repeating pattern along the orbit as a function of the ANX time; the antenna mispointing increases, reaching a peak, and then it starts to gradually decline until reaching a minimum, after which it begins to increase again, ultimately reaching its maximum peak in the next orbital cycle. Applying a 250 km running window and performing a weekly average effectively smooths the data, revealing the underlying trend with an amplitude of approximately 0.006° (0.8 m s^{-1}). Both the phase and amplitude of this trend shift over the course of the year. In June, the mispointing peak reaches 0.006° before the 20 min mark, whereas the minimum is around 0° at the 55 min mark. In February, the mispointing trend remains similar but appears shifted by nearly 10 min in time, with the amplitude's maximum and minimum reaching approximately 0.004 and −0.002°, respectively. This amplitude span of 0.006° is significant because it corresponds to a Doppler velocity shift of 0.8 m s^{-1}. The deviation of individual 250 km along-track averaged measurements from their respective fits exhibits a second-order residual with a standard deviation of approximately 0.00055° (0.07 m s^{-1}). Additionally, individual orbits occasionally diverge from their weekly averaged trend, likely due to variations in solar radiation (Bard and Frank, 2006) affecting the antenna deformation pattern. Because the presence of thermoelastic distortions cannot be excluded, the effect of sunlight rays reaching

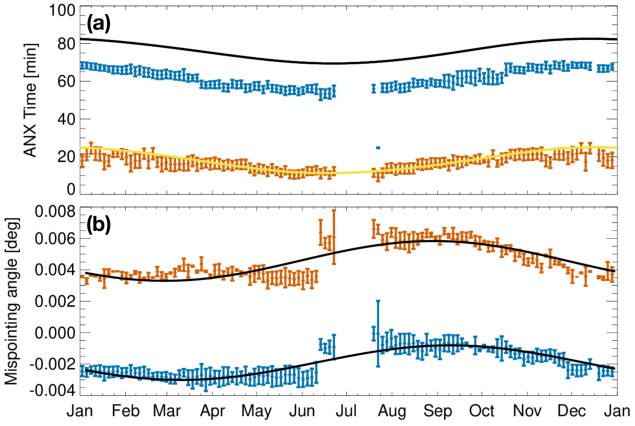

Figure 5. Panel **(a)** shows the ANX time of the minimum (blue) and maximum (red) angles of the weekly averaged mispointing trends as a function of the time of year. The yellow and black lines denote the spacecraft's daylight entry and exit times, respectively. Panel **(b)** presents the minimum (blue) and maximum (red) angles of the weekly averaged mispointing trends as a function of the time of year, with black lines representing fitted harmonics. In both panels, the vertical bars indicate the standard deviation. Gaps correspond to periods not yet covered by CPR measurements.

the antenna must be considered, specifically the spacecraft daylight entry and exit times, along with the solar azimuth angle and their seasonal variations, which are expected to cause the shifts in time and amplitude.

Another important point worth noting is the similarity with the along-track component of the previously introduced geolocation assessment. Both analyses yield results of the same order of magnitude, with differences arising from methodological differences between the two approaches.

To fully characterize the evolution of the CPR antenna mispointing throughout the year, the minimum and maxi-

mum values of each weekly averaged mispointing trend are tracked and analyzed as a function of the time of year. The results are highlighted in Fig. 5.

These results illustrate a dependence between solar illumination and the mispointing cycle, supporting the hypothesis that thermoelastic distortions affect the CPR antenna pointing. The mispointing trend reaches its maximum when the spacecraft enters daylight and its minimum about 12 min before exiting daylight. The observed increase in mispointing in Fig. 4 corresponds to the eclipse phase of the orbit, while the gradual decline occurs during the sunlit phase. Additionally, the mispointing amplitude varies throughout the year. During winter in the Northern Hemisphere, both the minimum and maximum mispointing values are at their lowest, whereas their magnitudes increase during the summer months. This analysis indicates that both the time and amplitude shifts observed in Fig. 4 can be explained by seasonal variations, specifically the changes in solar elevation – affecting the spacecraft's entry and exit times – and solar azimuth, which influences the incidence of sunlight on the antenna. These variations evolve systematically with the ANX time throughout the year and thus are fully predictable.

Figure 6 provides a visualization of EarthCARE's orientation relative to sunlight during its daylight phase, helping explain the antenna mispointing trends. Figure 6a shows the spacecraft just a few moments after entering daylight, where sunlight rays (yellow line) strike the antenna perpendicularly. This direct solar illumination likely causes the rapid change in the mispointing angle trend observed early in the daylight phase (Fig. 4b and c). Figure 4b illustrates the spacecraft shortly before exiting daylight. At this point, sunlight is partially blocked by the spacecraft body and solar panels, reducing direct exposure to the antenna. This shading effect seems to contribute to the second change in trend, as observed after the decline toward near-zero values (Fig. 4f and g). The transition between these two phases – direct exposure upon entry and gradual shading before exit – aligns with the periodic variations in the mispointing angle and highlights the impact of prolonged solar illumination and its absence, consistent with thermoelastic distortions. The delays or offsets in the change in trends are likely a result of the time required for thermal effects to propagate through the antenna structure.

The information presented in Fig. 5 is used to establish a normalized parameterization of the antenna mispointing pattern in Lagrangian coordinates, with 1 January as the reference time. This parameterization accounts for the systematic seasonal variation that affects both phase and amplitude shifts. The resulting fit, shown in Fig. 7, provides a refined characterization of the climatological antenna mispointing pattern.

This parameterization serves as a climatological reference for modeling the CPR antenna mispointing and can be used to identify the actual mispointing on an orbit-to-orbit basis. The phase and amplitude of the normalized fit are adjusted throughout the year, leveraging the information depicted in Fig. 5. To determine the actual mispointing angle at any given time, the normalized mispointing value is first shifted based on the difference of the daylight entry time relative to the reference date (1 January) and then scaled according to the seasonal amplitude variation. This ensures that the final estimate accurately reflects the expected mispointing trend over the year.

A detailed description of how to apply this correction to the radar signal – including the look-up table (LUT) derived in this study, the mathematical formulation, and the implementation steps – is provided in the "Data availability" section and Appendix A.

It is also worth noting that the previously mentioned second-order residual of 0.00055° (1.98 arcsec), observed in the individual weekly orbital assessments, is also reflected in the variability of the normalized trend. Specifically, the standard deviation is 0.9, which, when multiplied by the average amplitude of 0.006° (Fig. 5b), results in 0.00055°, which corresponds to $7\,\mathrm{cm\,s^{-1}}$ in the Doppler velocity space. The convergence of these values suggests that the applied transformations accurately preserve the structure of the mispointing variability.

When applying this climatological reference to correct the EarthCARE CPR dataset, it is also essential to account for other sources of uncertainty and orbit-to-orbit variations. As previously mentioned, some orbits occasionally diverge from the expected trend, suggesting that the antenna does not always deform in the exact same way. To mitigate residual biases and ensure a highly adaptive and robust correction methodology, a final optimization step minimizes the residuals relative to the mispointing angles derived from the ingested 250 km along-track averaged surface Doppler velocity observations.

This procedure aims to further adjust and reduce the residuals. The amplitude limits are systematically perturbed in small increments of 0.0001° over a range spanning twice the measured standard deviation (0.0011°). For each perturbation pair, the mean absolute difference (MAD) between the reference and the orbital observations is computed. After evaluating all combinations, the optimal amplitude limits are determined by selecting the pair that minimizes the MAD. To evaluate its effectiveness, this process has been applied to approximately 3000 orbits. A comparison between the modeled mispointing trend and the mispointing angles derived from the ingested observations shows that the 90th percentile of residuals remains below 0.00077° (2.77 arcsec, $\sim 10\,\mathrm{cm\,s^{-1}}$), highlighting the effectiveness and precision of the suggested method for correcting the antenna mispointing.

5 Effect on ice clouds

As a further evaluation, the effects of CPR antenna mispointing and the proposed correction methodology are analyzed on Doppler velocity measurements of ice clouds. For this

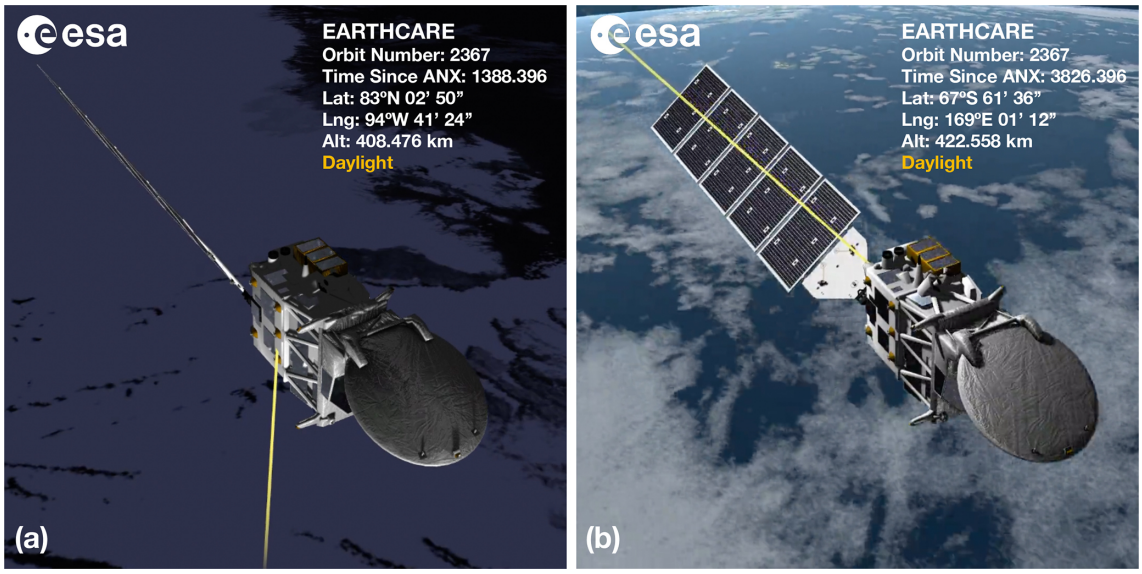

Figure 6. 3D model of EarthCARE from the Satellite Mission Editor and Player (SAMI) software package distributed by ESA. Panel **(a)** shows the satellite a few seconds after entering daylight, while panel **(b)** depicts it a few minutes before exiting daylight on 1 October 2024. The yellow line represents the direction of sunlight rays reaching the satellite.

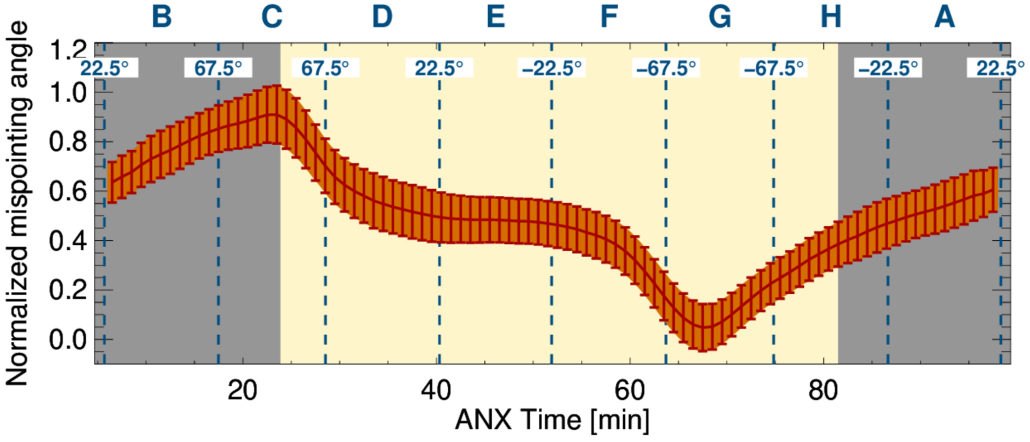

Figure 7. Normalized antenna mispointing angle as a function of the ANX time, aligned with the spacecraft's daily daylight cycle as of 1 January. The angle is normalized according to the seasonal amplitude variation. The red lines and shading denote the mean and standard deviation, and the yellow background represents the spacecraft daylight coverage time. The letters on top correspond to the frame IDs, which denote the different segments of the orbit, each spanning a specific latitude and time range marked by the dashed vertical lines, with the corresponding latitude values displayed above them.

purpose, the quality-controlled mean Doppler velocity estimates and radar reflectivity of ice clouds from the C-CD and C-FMR product (Kollias et al., 2023) are collected from one of the time periods where the antenna mispointing is at its maximum – January 2025. The C-CD processing includes a correction for NUBF effects, integration over 4 km along-track and 500 m in height, and a correction for velocity folding, whereas the C-FMR processing applies a filtering mask for non-meteorological echoes and a correction for gaseous attenuation. Leveraging this information, the evaluation is performed using the global reflectivity–Doppler velocity (Z–V) relationship of ice clouds between the temperatures of -30 and $-40°$. The results of the analysis are depicted in Fig. 8.

The analysis depicted in Fig. 8 confirms the effectiveness of the antenna pointing correction. With the correction applied, the Z–V relationships become consistent across all different segments of the orbit, identified by the unique frame IDs. In contrast, without the correction, the Doppler velocities exhibit segment-dependent biases, with frames G and C being the most affected by positive and negative biases, respectively. This result agrees with the initial assess-

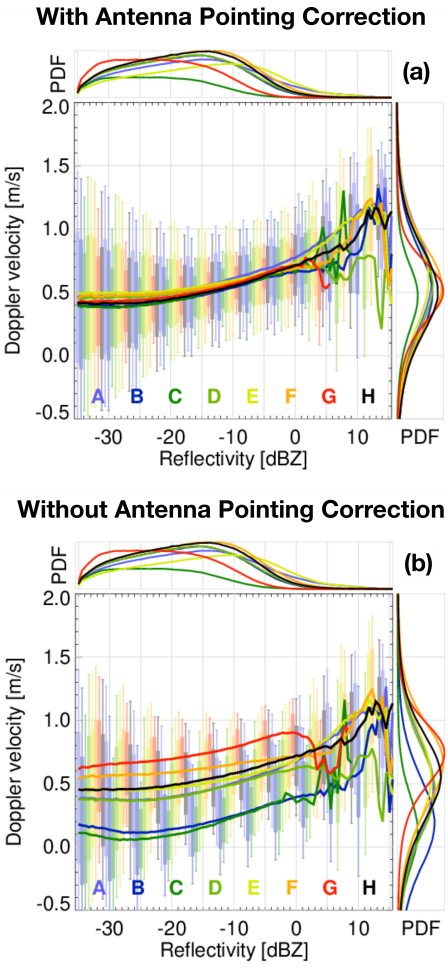

Figure 8. Reflectivity–Doppler velocity (Z–V) relationships of ice clouds for temperatures between −30 and −40 °C for the month of January 2025. Panels **(a)** and **(b)** depict the Z–V relationships with and without the antenna pointing correction, respectively. Each color represents a different frame ID, while the vertical bars indicate the 10th, 25th, 75th, and 90th percentiles, and the solid lines represent the median. The overlaid probability density functions (PDF) on the top and right axes illustrate the distribution of reflectivity and Doppler velocity samples contributing to each range. Note that the C-CD L2a product inverts the velocity sign with respect to the C-NOM L1b product.

ment shown in Fig. 4. Additionally, the figure also illustrates the Doppler velocity variability under different signal-to-noise ratio (SNR) conditions. Below −21 dBZ (SNR = 0), the Doppler velocity variability becomes significantly large, indicating a reduced measurement reliability.

Another important aspect worth mentioning is that the well-characterized Z–V climatological relationships of ice clouds from the EarthCARE dataset can serve as an additional reference for assessing the antenna mispointing (Battaglia and Kollias, 2015b). These measurements provide a valuable source of information that can complement surface Doppler measurements, increasing the number of samples in the orbit-to-orbit corrections and further improving their accuracy. Any deviation from the Z–V climatological relationships may indicate a potential antenna mispointing.

6 Summary

This study highlights the critical role of precise geolocation and antenna pointing correction in ensuring the quality of EarthCARE's CPR observations, particularly in minimizing errors in Doppler velocity measurements.

A similar challenge was encountered in the Aeolus Doppler lidar mission, where thermoelastic deformations led to orbit- and seasonally dependent pointing biases, reinforcing the importance of monitoring structural responses to thermal effects in active remote sensing systems.

Through a comprehensive geolocation assessment leveraging natural targets such as coastlines and terrains with significant elevation gradients, we demonstrate that the CPR instrument is properly geolocated within the specified mission requirements. However, the examination of surface Doppler velocity measurements reveals systematic mispointing trends influenced by seasonal variations and thermoelastic distortions of the antenna structure.

The characterization of these mispointing trends, based on surface Doppler velocity measurements, indicates a cyclic pattern in the along-track mispointing angle, which correlates with the spacecraft's daylight cycle. This mispointing is shown to be driven by thermoelastic effects resulting from variations in solar illumination, with peak deviations occurring near daylight entry and a few minutes before exit. The observed biases are quantified and parameterized to a climatological mispointing reference model, which accounts for both phase and amplitude variations throughout the year. This parameterization allows correcting the CPR data to within 5–7 $\mathrm{cm\,s^{-1}}$ (the 90th percentile is below 10 $\mathrm{cm\,s^{-1}}$) precision, significantly reducing Doppler velocity biases.

The impact of the antenna mispointing on CPR Doppler velocity measurements is further validated through ice cloud climatology. Prior to correction, the observed reflectivity–Doppler velocity relationships exhibit systematic biases, which are effectively removed after applying the mispointing correction. This improvement confirms that the corrected Doppler velocity data provide a more accurate representation of atmospheric dynamics, ensuring the integrity of EarthCARE's mission objectives.

Overall, the methodologies developed and applied in this study establish a robust framework for geolocation validation and antenna pointing correction that will benefit the ongoing calibration and validation efforts of the EarthCARE mission and will be applied in the level 2 processors, i.e., C-APC and C-PRO (Kollias et al., 2023). The findings underscore the necessity of continuous monitoring and refinement of mispointing corrections to maintain the high accuracy required for Doppler velocity measurements, ultimately enhancing the

scientific utility of EarthCARE's CPR observations in studying cloud microphysics and precipitation processes.

Appendix A

This section describes the application of the antenna mispointing look-up table (LUT) to correct the EarthCARE CPR Level 1b Doppler velocity data using the climatological fit of the CPR antenna mispointing presented in this study. The correction is applied directly to the complex lag-1 autocovariance of the pulse-pair radar signal, prior to Doppler velocity derivation.

Performing the correction directly in Doppler velocity space requires careful handling of Nyquist folding effects, particularly at high PRF. Even small mispointing angles can induce phase shifts that exceed the Nyquist limit, leading to velocity aliasing. Instead, applying the correction at the level of the complex radar signal avoids this ambiguity and ensures phase continuity.

A1 Overview

The EarthCARE CPR Doppler velocity is derived from the phase angle of the lag-1 autocovariance of the IQ signal. This phase shift between consecutive pulses encodes the Doppler frequency and is given by:

$$V = \frac{\lambda \cdot \mathrm{PRF}}{4\pi} \cdot \theta_{\mathrm{nom}}, \tag{A1}$$

where λ is the radar wavelength, PRF is the pulse repetition frequency, and θ_{nom} is the phase angle of the complex lag-1 autocovariance, computed from its real ($R[R]$) and imaginary ($I[R]$) components:

$$\theta_{\mathrm{nom}} = \mathrm{atan}(I[R], R[R]). \tag{A2}$$

A2 Line-of-sight correction

A correction must first be applied for line-of-sight (LOS) contamination resulting from the satellite's motion projected onto the CPR beam direction. This effect is not accounted for in the pulse-pair radar signal reported in the L1b. The LOS-projected velocity (V_{LOS}) is computed as follows:

$$V_{\mathrm{LOS}} = V_{\mathrm{sat}} \cdot \sin(\theta_{\mathrm{ADS}}), \tag{A3}$$

where V_{sat} is the satellite velocity in Earth-centered, Earth-fixed (ECEF) coordinates and θ_{ADS} is the antenna pitch angle reported by the Attitude Determination System (ADS). This LOS velocity introduces a phase shift in the measured signal:

$$\theta_{\mathrm{LOS}} = \frac{4\pi \cdot V_{\mathrm{LOS}}}{\lambda \cdot \mathrm{PRF}}. \tag{A4}$$

The phase correction is applied by subtracting this LOS-induced phase (θ_{LOS}) from the nominal measured phase:

$$\theta_{\mathrm{LOS\text{-}CORR}} = \theta_{\mathrm{nom}} - \theta_{\mathrm{LOS}}. \tag{A5}$$

To correct the complex lag-1 autocovariance, the real and imaginary components of the lag-1 autocovariance are recomputed using the corrected phase:

$$I[R]_{\mathrm{LOS\text{-}CORR}} = |R[R] + j \cdot I[R]| \cdot \sin(\theta_{\mathrm{LOS\text{-}CORR}}), \tag{A6}$$

$$R[R]_{\mathrm{LOS\text{-}CORR}} = |R[R] + j \cdot I[R]| \cdot \cos(\theta_{\mathrm{LOS\text{-}CORR}}). \tag{A7}$$

The Doppler velocity corrected for LOS contamination can then be obtained by applying Eqs. (A2) and (A1) to the updated complex radar signal defined by Eqs. (A6) and (A7).

A3 Antenna mispointing correction

The antenna mispointing LUT provides a normalized mispointing pattern as a function of the ANX time, along with the corresponding seasonal amplitude and phase shifts. These parameters define a climatological model of the antenna mispointing that evolves smoothly over the course of the year. At a given ANX time (t) and day-of-year (d), the mispointing correction is computed as follows:

$$\theta_{\mathrm{APC}}(t,d) = m_{\mathrm{norm}}(t + \delta t_{\phi}(d)) \cdot (A_{\mathrm{max}}(d) - A_{\mathrm{min}}(d)) + A_{\mathrm{min}}(d), \tag{A8}$$

where $m_{\mathrm{norm}}(t)$ is the normalized mispointing pattern, $\delta t_{\phi}(d)$ is the seasonal phase shift, and $A_{\mathrm{min}}(d)$ and $A_{\mathrm{max}}(d)$ are the minimum and maximum seasonal amplitude bounds.

This parameterization allows the reconstruction and correction of the antenna mispointing angle across the orbit and throughout the year. Once the mispointing angle θ_{APC} is known, it can be converted to a Doppler phase correction following the same approach described in the LOS correction section.

A4 Implementation notes

The LUT information must be applied to each specific frame by interpolation. All required variables are found in the CPR L1b data product (C-NOM), including *rayHeaderLambda* (λ), *rayStatusPrf* (PRF), *covarianceCoeff* ($R[R]$ and $I[R]$), *pitchAngle* (θ_{ADS}), *satelliteVelocityX*, *satelliteVelocityY*, *satelliteVelocityZ* (components of V_{sat}), *profileTime*, and ANXTime(t).

In the CPR L2a processing (C-APC), an additional optimization step is applied to minimize the residuals between the climatological mispointing model and the mispointing angles inferred from the raw measured surface Doppler velocity measurements. This step refines the amplitude scaling for each orbit and ensures that residual Doppler velocity biases are reduced within 5–7 $\mathrm{cm\,s^{-1}}$ (the 90th percentile is below 10 $\mathrm{cm\,s^{-1}}$).

This correction is valid at the time of reviewing this paper (June 2025). Future versions of the CPR L1b data product may include antenna mispointing corrections directly in the processing chain. Additionally, updates to the orbital specifications may affect the accuracy of this correction. Users are

advised to consult the latest product specifications and orbital parameters before applying this method.

Data availability. The antenna mispointing correction LUT derived in this study is available at Zenodo (https://doi.org/10.5281/zenodo.15740762; Puigdomènech Treserras et al., 2025). Instructions for applying the correction to EarthCARE CPR L1b data are provided in the Appendix A.

Author contributions. BPT developed the geolocation assessment and antenna pointing correction tools, performed the analysis, generated the figures, and drafted a version of the paper. PK, AB, HN, and ST contributed to the evaluation of the results and provided feedback on the writing.

Competing interests. The contact author has declared that none of the authors has any competing interests.

Disclaimer. Publisher's note: Copernicus Publications remains neutral with regard to jurisdictional claims made in the text, published maps, institutional affiliations, or any other geographical representation in this paper. While Copernicus Publications makes every effort to include appropriate place names, the final responsibility lies with the authors.

Special issue statement. This article is part of the special issue "Early results from EarthCARE (AMT/ACP/GMD inter-journal SI)". It is not associated with a conference.

Acknowledgements. Portions of this work were presented at the EarthCARE CAL/VAL Workshop 1, held at ESA ESRIN, Frascati, Italy, in March 2025.

Financial support. Work done by Bernat Puigdomènech Treserras and Pavlos Kollias was supported by the European Space Agency (ESA) under the Clouds, Aerosol, Radiation – Development of INtegrated ALgorithms (CARDINAL) project (grant no. RFQ/3-17010/20/NL/AD). Part of the research described in this paper was carried out at the Jet Propulsion Laboratory, California Institute of Technology, under contract with the National Aeronautics and Space Administration.

Review statement. This paper was edited by Thorsten Fehr and reviewed by two anonymous referees.

References

Bard, E. and Frank, M.: Climate change and solar variability: What's new under the sun?, Earth and Planetary Science Letters, 248, https://doi.org/10.1016/j.epsl.2006.06.016, 2006.

Battaglia, A. and Kollias, P.: Impact of Receiver Saturation on Surface Doppler Velocity Measurements From the EarthCARE Cloud Profiling Radar, IEEE Transactions on Geoscience and Remote Sensing, 53, 1205–1212, https://doi.org/10.1109/TGRS.2014.2335896, 2015a.

Battaglia, A. and Kollias, P.: Using Ice Clouds for Mitigating the EarthCARE Doppler Radar Mispointing, IEEE Transactions on Geoscience and Remote Sensing, 53, 2079–2085, https://doi.org/10.1109/TGRS.2014.2353219, 2015b.

Battaglia, A., Kollias, P., Dhillon, R., Roy, R., Tanelli, S., Lamer, K., Grecu, M., Lebsock, M., Watters, D., Mroz, K., Heymsfield, G., Li, L., and Furukawa, K.: Spaceborne cloud and precipitation radars: Status, challenges, and ways forward, Reviews of Geophysics, 58, e2019RG000686, https://doi.org/10.1029/2019RG000686, 2020.

Burns, D., Kollias, P., Tatarevic, A., Battaglia, A., and Tanelli, S.: The performance of the EarthCARE Cloud Profiling Radar in marine stratiform clouds, J. Geophys. Res.-Atmos., 121, 14525–14537, https://doi.org/10.1002/2016JD025090, 2016.

Cole, J. N. S., Barker, H. W., Qu, Z., Villefranque, N., and Shephard, M. W.: Broadband radiative quantities for the EarthCARE mission: the ACM-COM and ACM-RT products, Atmos. Meas. Tech., 16, 4271–4288, https://doi.org/10.5194/amt-16-4271-2023, 2023.

Haynes, J. M., L'Ecuyer, T. S., Stephens, G. L., Miller, S. D., Mitrescu, C., Wood, N. B., and Tanelli, S.: Rainfall retrieval over the ocean with spaceborne W-band radar, J. Geophys. Res., 114, D00A22, https://doi.org/10.1029/2008JD009973, 2009.

Illingworth, A. J., Barker, H. W., Beljaars, A., Ceccaldi, M., Chepfer, H., Clerbaux, N., Cole, J., Delanoë, J., Domenech, C., Donovan, D. P., Fukuda, S., Hirakata, M., Hogan, R. J., Huenerbein, A., Kollias, P., Kubota, T., Nakajima, T., Nakajima, T. Y., Nishizawa, T., Ohno, Y., Okamoto, H., Oki, R., Sato, K., Satoh, M., Shephard, M. W., Velázquez-Blázquez, A., Wandinger, U., Wehr, T., and van Zadelhoff, G.-J.: The EarthCARE Satellite: The Next Step Forward in Global Measurements of Clouds, Aerosols, Precipitation, and Radiation, Bull. Amer. Meteor. Soc., 96, 1311–1332, https://doi.org/10.1175/BAMS-D-12-00227.1, 2015.

Irbah, A., Delanoë, J., van Zadelhoff, G.-J., Donovan, D. P., Kollias, P., Puigdomènech Treserras, B., Mason, S., Hogan, R. J., and Tatarevic, A.: The classification of atmospheric hydrometeors and aerosols from the EarthCARE radar and lidar: the A-TC, C-TC and AC-TC products, Atmos. Meas. Tech., 16, 2795–2820, https://doi.org/10.5194/amt-16-2795-2023, 2023.

Kanitz, T., Lochard, J., Marshall, J., McGoldrick, P., Lecrenier, O., Bravetti, P., Reitebuch, O., Rennie, M., Wernham, D., and Elfving, A.: Aeolus first light: first glimpse, in: International Conference on Space Optics – ICSO 2018, Chania, Greece, 111801R, https://doi.org/10.1117/12.2535982, 2019.

Kobayashi, S. and Kumagai, H.: Doppler Velocity from Sea Surface on the Spaceborne and Airborne Weather Radars, J. Atmos. Oceanic Technol., 20, 372–381, https://doi.org/10.1175/1520-0426(2003)020<0372:DVFSSO>2.0.CO;2, 2003.

Kollias, P., Tanelli, S., Battaglia, A., and Tatarevic, A.: Evaluation of EarthCARE Cloud Profiling Radar Doppler Velocity Measurements in Particle Sedimentation Regimes, J. Atmos. Ocean. Technol., 31, 366–386, https://doi.org/10.1175/JTECH-D-11-00202.1, 2014.

Kollias, P., Battaglia, A., Lamer, K., Puigdomènech Treserras, B. and Braun, S. A.: Mind the Gap – Part 3: Doppler Velocity Measurements From Space, Front. Remote Sens., 3, 860284, https://doi.org/10.3389/frsen.2022.860284, 2022.

Kollias, P., Puidgomènech Treserras, B., Battaglia, A., Borque, P. C., and Tatarevic, A.: Processing reflectivity and Doppler velocity from EarthCARE's cloud-profiling radar: the C-FMR, C-CD and C-APC products, Atmos. Meas. Tech., 16, 1901–1914, https://doi.org/10.5194/amt-16-1901-2023, 2023.

Manconi, F., Battaglia, A., and Kollias, P.: Characterization of surface clutter signal in the presence of orography for a spaceborne conically scanning W-band Doppler radar, Atmos. Meas. Tech., 18, 2295–2310, https://doi.org/10.5194/amt-18-2295-2025, 2025.

Mason, S. L., Hogan, R. J., Bozzo, A., and Pounder, N. L.: A unified synergistic retrieval of clouds, aerosols, and precipitation from EarthCARE: the ACM-CAP product, Atmos. Meas. Tech., 16, 3459–3486, https://doi.org/10.5194/amt-16-3459-2023, 2023.

Puigdomènech Treserras, B. and Kollias, P.: An improved geolocation methodology for spaceborne radar and lidar systems, Atmos. Meas. Tech., 17, 6301–6314, https://doi.org/10.5194/amt-17-6301-2024, 2024.

Puigdomènech Treserras, B., Kollias, P., Battaglia, A., Tanelli, S., and Nakatsuka, H.: EarthCARE CPR Antenna Mispointing Correction LUT, Zenodo [data set], https://doi.org/10.5281/zenodo.15740762, 2025.

Reitebuch, O., Lemmerz, C., Lux, O., Marksteiner, U., Rahm, S., Weiler, F., Witschas, B., Meringer, M., Schmidt, K., Huber, D., Nikolaus, I., Geiss, A., Vaughan, M., Dabas, A., Flament, T., Stieglitz, H., Isaksen, L., Rennie, M., Kloe, J. de, Marseille, G.-J., Stoffelen, A., Wernham, D., Kanitz, T., Straume, A.-G., Fehr, T., Bismarck, J. von, Floberghagen, R., and Parrinello, T.: Initial Assessment of the Performance of the First Wind Lidar in Space on Aeolus, EPJ Web Conf., 237, 01010, https://doi.org/10.1051/epjconf/202023701010, 2020.

Rennie, M., Isaksen, L., Weiler, F., de Kloe, J., Kanitz, Th., and Reitebuch, O.: The impact of Aeolus wind retrievals in ECMWF global weather forecasts, Q. J. Roy. Meteor. Soc., 147, 3555–3586, https://doi.org/10.1002/qj.4142, 2021.

Scarsi, F. E., Battaglia, A., Tridon, F., Martire, P., Dhillon, R., and Illingworth, A.: Mispointing characterization and Doppler velocity correction for the conically scanning WIVERN Doppler radar, Atmos. Meas. Tech., 17, 499–514, https://doi.org/10.5194/amt-17-499-2024, 2024.

Stephens, G. L., Vane, D. G., Boain, R. J., Mace, G. G., Sassen, K., Wang, Z., Illingworth, A. J., O'connor, E. J., Rossow, W. B., Durden, S. L., Miller, S. D., Austin, R. T., Benedetti, A., and Mitrescu, C. A.: THE CLOUDSAT MISSION AND THE A-TRAIN, B. Am. Meteorol. Soc., 83, 1771–1790, https://doi.org/10.1175/BAMS-83-12-1771, 2002.

Sy, O., Tanelli, S.: Dynamic Retrievals From Spaceborne Doppler Radar Measurements: The CConDoR Approach, IEEE Transactions on Geoscience and Remote Sensing, 60, 5115916, https://doi.org/10.1109/TGRS.2022.3192177, 2022.

Sy, O., Tanelli, S., Takahashi, N., Ohno, Y., Horie, H., and Kollias, P.: Simulation of EarthCARE Spaceborne Doppler Radar Products Using Ground-Based and Airborne Data: Effects of Aliasing and Nonuniform Beam-Filling, IEEE T. Geosci. Remote, 52, 1463–1479, https://doi.org/10.1109/TGRS.2013.2251639, 2014.

Tanelli, S., Im, E., Durden, S. L., Facheris, L., and Giuli, D.: The effects of nonuniform beam filling on vertical rainfall velocity measurements with a spaceborne Doppler radar, J. Atmos. Ocean. Technol., 19, 1019–1034, https://doi.org/10.1175/1520-0426(2002)019<1019:TEONBF>2.0.CO;2, 2002.

Tanelli, S., Im, E., Kobayashi, S., Mascelloni, R., and Facheris, L.: Spaceborne Doppler Radar Measurements of Rainfall: Correction of Errors Induced by Pointing Uncertainties, J. Atmos. Oceanic Technol., 22, 1676–1690, https://doi.org/10.1175/JTECH1797.1, 2005.

Tanelli, S., Durden, S. L., Im, E., Pak, K. S., Reinke, D. G., Partain, P., Haynes, J. M., and Marchand, R. T.: CloudSat's Cloud Profiling Radar After Two Years in Orbit: Performance, Calibration, and Processing, IEEE T. Geosci. Remote, 46, 3560–3573, https://doi.org/10.1109/TGRS.2008.2002030, 2008.

Tanelli, S., Im, E., Durden, S. L., Facheris, L., and Giuli, D.: The Effects of Nonuniform Beam Filling on Vertical Rainfall Velocity Measurements with a Spaceborne Doppler Radar, J. Atmos. Oceanic Technol., 19, 1019–1034, https://doi.org/10.1175/1520-0426(2002)019<1019:TEONBF>2.0.CO;2, 2002.

Testud, J., Hildebrand, P. H., and Lee, W.: A procedure to correct airborne Doppler radar for navigation errors using the echo returned from the earth's surface, J. Atmos. Oceanic Technol., 12, 800–820, https://doi.org/10.1175/1520-0426(1995)012<0800:APTCAD>2.0.CO;2, 1995.

Wehr, T., Kubota, T., Tzeremes, G., Wallace, K., Nakatsuka, H., Ohno, Y., Koopman, R., Rusli, S., Kikuchi, M., Eisinger, M., Tanaka, T., Taga, M., Deghaye, P., Tomita, E., and Bernaerts, D.: The EarthCARE mission – science and system overview, Atmos. Meas. Tech., 16, 3581–3608, https://doi.org/10.5194/amt-16-3581-2023, 2023.

Weiler, F., Rennie, M., Kanitz, T., Isaksen, L., Checa, E., de Kloe, J., Okunde, N., and Reitebuch, O.: Correction of wind bias for the lidar on board Aeolus using telescope temperatures, Atmos. Meas. Tech., 14, 7167–7185, https://doi.org/10.5194/amt-14-7167-2021, 2021.